HHS Public Access

Author manuscript

Nanoscale. Author manuscript; available in PMC 2017 July 14.

Published in final edited form as:

Nanoscale. 2016 July 14; 8(28): 13740–13754. doi:10.1039/c6nr02618d.

Gold silver alloy nanoparticles (GSAN): an imaging probe for breast cancer screening with dual-energy mammography or computed tomography

Pratap C. Naha[1], **Kristen C. Lau**[1], **Jessica C. Hsu**[1,2], **Maryam Hajfathalian**[3], **Shaameen Mian**[2], **Peter Chhour**[1,2], **Lahari Uppuluri**[1], **Elizabeth S. McDonald**[1], **Andrew D. A. Maidment**[1], and **David P. Cormode**[1,2,4,*]

[1]Department of Radiology, University of Pennsylvania 3400 Spruce St, 1 Silverstein, Philadelphia, PA 19104, USA

[2]Department of Bioengineering, University of Pennsylvania, Philadelphia, PA, USA

[3]Department of Mechanical Engineering, Temple University, Philadelphia, PA, USA

[4]Department of Cardiology, University of Pennsylvania, Philadelphia, PA, USA

Abstract

Earlier detection of breast cancer reduces mortality from this disease. As a result, the development of better screening techniques is a topic of intense interest. Contrast-enhanced dual-energy mammography (DEM) is a novel technique that has improved sensitivity for cancer detection. However, the development of contrast agents for this technique is in its infancy. We herein report gold-silver alloy nanoparticles (GSAN) that have potent DEM contrast properties and improved biocompatibility. GSAN formulations containing a range of gold:silver ratios and capped with m-PEG were synthesized and characterized using various analytical methods. DEM and computed tomography (CT) phantom imaging showed that GSAN produced robust contrast that was comparable to silver alone. Cell viability, reactive oxygen species generation and DNA damage results revealed that the formulations with 30% or higher gold content are cytocompatible to Hep G2 and J774A.1 cells. *In vivo* imaging was performed in mice with and without breast tumors. The results showed that GSAN produce strong DEM and CT contrast and accumulated in tumors. Furthermore, both *in vivo* imaging and *ex vivo* analysis indicated the excretion of GSAN via both urine and feces. In summary, GSAN produce strong DEM and CT contrast, and has potential for both blood pool imaging and for breast cancer screening.

Graphical abstract

*Corresponding author Tel: 215-615-4656, Fax: 240-368-8096, david.cormode@uphs.upenn.edu.

Conflicts of interest

We have no conflict of interest to declare.

Supporting information

Reactive oxygen species generation and DNA damage methods, stability of GSAN in PBS, step phantom images and a DEM image of a gold nanoparticle phantom, GSAN CT phantom results are presented in the supporting information.

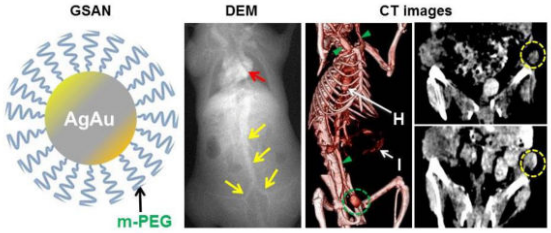

Keywords

gold nanoparticles; silver nanoparticles; dual-energy mammography; computed tomography; contrast agents; breast cancer screening

Introduction

Mammography is an x-ray based imaging technique that is used to screen for breast cancer.[1] Population screening with mammography is estimated to reduce mortality due to breast cancer by at least 15%,[2] due to early detection, allowing early intervention and thereby preventing progression and metastasis.[3] Nevertheless, numerous lesions remain undetected with current mammography techniques due to issues such as high breast density,[4] allowing tumors to progress and thereby resulting in worse outcomes. About half of women are classed as having high breast density.[5] The sensitivity of mammography for women with low density breasts is 88%, whereas it is only 30-60% in women with high breast density.[6,7] Dual-energy mammography (DEM) aims to distinguish tumors from adipose/glandular tissue via the different attenuation of materials at different x-ray energies. Contrast agents are used with DEM to highlight tumors due to their increased blood flow.[6] In this technique, two mammograms are acquired in rapid succession using two different x-ray tube voltages and beam filters.[3,4] While all soft tissues have similar ratios of attenuation between the low and high energy x-ray images, the contrast agents used have higher attenuation in the high energy window, due to their k-edge.[8] A logarithmically weighted image subtraction is done to create a DE image. The signal from the breast tissue is suppressed and that from the contrast agent is enhanced. The result is that tumors have very high conspicuity.

The primary form of contrast agent for x-ray based imaging is iodinated small molecules such as iopamidol or iodixanol.[9] However, these iodinated agents have a number of drawbacks including patient allergic reactions and contra-indication for use with renal insufficiency,[10,11] due to the risk of contrast-induced nephropathy.[12,13] In addition, the half-lives of these agents are very short, necessitating high doses and swift post-injection imaging. Also, the contrast produced by iodinated agents in DEM is suboptimal.[8] Most importantly, they have low specificity for tumors. Improved contrast agents are needed for tumor detection with DEM.

Nanoparticles have been proposed as contrast agents for breast cancer imaging with MRI, CT, photoacoustics and other techniques.[14-17] However, few of these agents are suited to breast cancer screening due to their complexity and specificity for certain sub-types of breast cancer. Furthermore, the development of contrast agents specifically designed for DEM has

barely been explored.[18] We and others have demonstrated that metal nanoparticles (such as gold and bismuth) are highly effective x-ray contrast agents.[19-26] Long-circulating nanoparticles accumulate in tumors due to extravasation from leaky, angiogenic blood vessels (the enhanced permeability and retention effect).[27] These nanoparticles produce strong contrast,[28,29] can be designed to circulate longer than iodinated contrast agents,[21,30,31] have a good safety profile,[32,33] and have been in clinical trials where no adverse effects were found.[34] Nevertheless, while gold nanoparticles (AuNP) produce strong x-ray contrast, they do not produce significant contrast for DEM since the k-edge of gold is at 80.7 keV, which is outside the range of energies used in mammography (~15-49 keV).

Recently, Karunamuni *et al.* identified that silver produces strong DEM contrast via simulations, as its k-edge at 25.5 keV is well-matched to the energies used in mammography.[8] It has been shown via experiments that silver nanoparticles produce 40% more contrast than iodine in DEM phantom imaging.[8] Proof of concept imaging was done in mice with silica-coated silver nanoparticles. The results confirmed that silver nanoparticles produce strong DEM contrast *in vivo*.[18] Therefore, silver is an excellent choice as an element upon which to base DEM specific contrast agents. However, the challenge for translation of silver nanoparticles is that they are not stable and oxidation may result in leaching of silver ions, causing a safety concern.[35] In comparison, gold nanoparticles have an excellent biocompatibility record[33,36] and cannot be oxidized *in vivo*. A few recent studies have probed the use of gold-silver core/shell nanoparticles as contrast agents for CT,[37-40] however none of those studies examined them as DEM contrast agents.

We hypothesized that inclusion of gold in silver nanoparticles would raise the oxidation potential of silver,[41] preventing leaching of silver ions and making the nanoparticles biocompatible. The gold would also improve the CT contrast properties of silver without sacrificing its favorable DEM contrast properties. In this study, we propose biocompatible gold-silver alloy nanoparticles (GSAN) as a novel contrast agent platform for both DEM and CT. We synthesized a range of GSAN formulations with varying molar ratios of silver and gold. These GSAN were characterized using dynamic light scattering (DLS), transmission electron microscopy (TEM), UV-visible spectroscopy and inductively coupled plasma optical emission spectroscopy (ICP-OES). The DEM and CT contrast properties of GSAN were investigated using a DEM system and a clinical CT scanner. *In vitro* cell viability studies were performed in Hep G2 and J774A.1 cells. *In vivo* imaging with DEM and CT was performed in mice with and without breast tumors to determine specific uptake. The biodistribution of GSAN was also determined.

Results and Discussion

Synthesis and characterization of GSAN

The GSAN formulations were synthesized by co-reduction of gold and silver salts using sodium borohydride and sodium citrate as reducing agents, as schematically depicted in Figure 1A. Six different formulations (termed Ag-100, Ag-90, Ag-80, Ag-70, Ag-60 and Ag-50) were synthesized by adjusting the molar ratio of gold and silver salts (Table 1). Ag-100 refers to the formulation where 100% silver was used in the synthesis, whereas Ag-90 refers to the formulation where 90% silver and 10% gold used in the synthesis and so

on. We successfully synthesized a range of GSAN (Figure 1). The particles were then capped with thiol-polyethylene glycol (PEG) with a methoxy end group to make them water soluble, stable in physiological buffer conditions and to enhance the *in vivo* blood circulation half-life. Citrate coated GSAN formulations were not found to be stable in PBS, however PEGylated GSAN formulations are stable in PBS. This is evidenced by aggregation and settling of the citrate coated GSAN when exposed to PBS, whereas PEG coated GSAN remained well suspended (Figure S1). We and others have previously observed that PEG provides gold nanoparticles with robust stability in biological media.[21,33] The color of the formulations changes from yellow to reddish-brown as the amount of gold increases (Figure 1B). This corresponded to a shift in the absorption maximum from 405 nm for Ag-100 to 485 nm for Ag-50 (Figure 1C).

We performed ICP-OES on all the GSAN formulations (Table 1). The results show that significant amounts of gold and silver were found in all the GSAN formulations except Ag-100. Energy dispersive x-ray spectroscopy result (Figure 2) confirmed the presence of silver and gold in the GSAN core. The yield of silver was found to be around 60-70% (Table 1). Typically, the percentage of silver in the final, purified formulation was slightly less than the percentage used in the synthesis.

TEM images of all formulations are presented in Figure 1D. The core size of all the GSAN formulations was found to be around ~5 nm (Table 1). The hydrodynamic diameters and zeta potentials of all the GSAN formulations were found to be around 16 nm and -20 mV, respectively (Table 1). The core and hydrodynamic diameters of all the GSAN formulations were similar, which is not surprising since the synthesis methodology was similar for all the formulations, with only the ratio of silver and gold salts varying. The coating material for the all the formulations was the same (i.e., m-PEG), therefore we did not see substantial differences in zeta potential values among the formulations.

Analysis of silver ion release and cytocompatibility *in vitro*

Unlike gold nanoparticles, silver nanoparticles are not inert in nature and can release silver ions, which can be a safety concern (Figure 3A). Our hypothesis is that making a gold-silver alloy nanoparticle would increase the reduction potential of silver atoms in the nanoparticle, minimize silver ion release and improve biocompatibility (Figure 3B). Silver ion leaching from all GSAN formulations was tested in two different dissolution media: DI water and simulated lysosomal fluid (pH 5) at 37 ºC. We performed this experiment in simulated lysosomal fluid because it has frequently been observed that nanoparticles are internalized into endosomes or lysosomes.[23,33] The lysosomal pH is slightly acidic, at around pH 5. Since others have shown that silver nanoparticles release more silver ions in acidic pH than neutral pH (7.4), probing lower pH is particularly important.[42,43] Therefore to probe pH dependence we performed silver ion release assays in these two different dispersion media (i.e. neutral and slightly acidic pH). We also performed cytotoxicity assays with two different cell types to probe the correlation of silver ion release data with cytotoxicity.

The release of silver ions from GSAN is shown in Figure 3C,D. In the case of DI water, more silver ions are released from silver nanoparticles (Ag 100) than GSAN formulations, with a trend that less silver is released the more gold is included in the formulation (Figure

3C). While about 0.6% of the silver was released from Ag-100 over 7 days, less than 0.1% release was seen from GSAN with 20% or more gold content. In simulated lysosomal fluid, Ag-100 and Ag-90 formulations release substantially more silver ions than the other GSAN formulations (Figure 3D). Curiously, Ag-90 released more silver ions than Ag-100, in contradiction to the results found in DI water. However this data matches well with results from the cell viability assay (see Fig 3E,F and below). Inclusion of 20% gold or more resulted in substantially decreased silver ion release, with 0.6% release or less, whereas 1.5% silver was released from Ag-100. As can be seen, more silver was released under acidic conditions than neutral conditions, which corresponds with the results found by others.[42,43]

To probe the effects of the observed silver ion release, we investigated the impact of the GSAN on the viability of J774A.1 and Hep G2 cells. All the GSAN formulations were found to be biocompatible with both cell lines except Ag-100 and Ag-90 (Figure 3E,F). Substantial reductions of J774A.1 and Hep G2 cell viability were observed when incubated with Ag-100 and Ag-90 formulations. This result is likely due to the greater amount of silver ions leached from these nanoparticles compared to other GSAN formulations. Ag-100 is a pure silver nanoparticle and the observed decreases in cell viability are in line with the results found by others.[42] Surprisingly, when incubated with Ag-90, the cell viability was even lower than for Ag-100. This result is in agreement, however, with the results found for silver ion release. More in-depth toxicological assessments of GSAN were performed via measurement of reactive oxygen species (ROS) generation and DNA damage studies in J774A.1 and Hep G2 cells. The results of these experiments are presented in Figure 4. Notably increased ROS generation was found in J774A.1 cells when incubated with Ag-100, Ag-90 and Ag-80 formulations, but not when incubated with Ag-70, Ag-60 and Ag-50. ROS generation was lower in HepG2 cells, but followed the same trend as for J774A.1, i.e. that Ag-100, Ag-90 and Ag-80 resulted in increased ROS generation, whereas Ag-70, Ag-60 and Ag-50 did not. DNA damage was found in J774A.1 and Hep G2 cells with the Ag-100, Ag-90 and Ag-80 formulations. However, only minor DNA damage was observed with both cell lines after 24 hour incubation with Ag-70. No DNA damage was found after incubations with the Ag-60 and Ag-50 formulations in either cell type.

Cell viability, ROS and DNA damage results indicate that inclusion of 30% or more gold in the formulation renders the GSAN biocompatible (Figure 3 and 4). Our hypothesis that inclusion of gold would reduce silver ion release and improve the biocompatibility of GSAN was proved correct.

Phantom imaging with DEM and CT

We performed phantom imaging to probe our second hypothesis: that the addition of gold would not affect the DEM contrast properties of silver. The generation of contrast in DEM depends on an element having a k-edge in the high energy window, e.g. from roughly 20-40 keV. Since the k-edge of gold is at 80.7 keV, it is not predicted to generate significant DEM contrast.[18,44] We investigated the DEM contrast properties of GSAN (at 16 mg Ag/ml) using a step phantom composed of materials that provide density ranging from that of 100% adipose to 100% glandular tissue. DEM images of this phantom acquired using a Hologic

Selenia Dimensions DEM system are presented in Figure 5A,B. Images were acquired at low energy (LE) and high energy (HE). A weighted logarithmic subtraction was performed to obtain dual-energy (DE) images (Figure 5A); it can be seen that the variation in the background signal has been greatly reduced and the contrast from the GSAN is enhanced.[18] Strong DEM contrast was observed from all the GSAN formulations and the silver nanoparticles (Figure 5B,C). The contrast-to-noise ratios (CNR) for all formulations were calculated from the DEM phantom images and are presented in Figure 5C. The results indicate that there is no significant difference in the CNR produced among all these formulations, as the concentration of silver was held constant for all the formulations (Figure 5C). We also performed gold nanoparticle phantom imaging with DEM, where little DEM contrast was observed (Figure S2), which is similar to our prior *in vivo* results.[18] Therefore, DEM phantom imaging results indicated that inclusion of gold in GSAN did not affect the DEM contrast properties created by silver.

The CT contrast properties of GSAN were evaluated using a clinical CT scanner (Siemens Force). An FDA-approved iodine-based contrast agent (iopamidol), gold nanoparticles and silver nitrate were also scanned as controls. Selected CT phantom images are presented in Figure 5D, while the CT attenuation rate of the different agents is presented in Figure 5E (the GSAN formulation is Ag-80). Data for additional GSAN formulations is presented in Figure S3 and is given in both units of HU/mg and HU/mM. The CT phantom results show that silver attenuates x-rays comparably to iopamidol, with the greatest attenuation at 80 kV, followed by a steady decline in attenuation as the x-ray tube voltage increases to 140 kV. This trend is in agreement with the attenuation predicted from data available from the National Institute of Standards – as the k-edge of silver is at 26 kV, silver should have stronger attenuation of lower energy x-rays than higher energy x-rays (Figure S4). These results indicate that silver has potential as a CT contrast agent in addition to a contrast agent for DEM. Gold has a k-edge at 80.7 kV, therefore it has stronger attenuation of high energy x-rays than low energy x-rays, hence the increase in attenuation from 80 to 120 kV. GSAN (Ag-90 to Ag-50 formulation) attenuates high energy x-rays with an absorption that is intermediate to those of gold and silver as it contains both of these elements (Figure S4). As can be seen, GSAN create CT contrast that is comparable with iodinated agents and gold nanoparticles and therefore could have use as a CT contrast agent.

In vivo imaging with DEM

In vitro analyses showed that several of the GSAN are biocompatible and phantom imaging results showed that GSAN produce strong contrast for DEM and CT. Based on these results we investigated the *in vivo* DEM and CT contrast properties and tumor accumulation efficiency of a GSAN formulation (Ag-60). We chose the Ag-60 formulation due to its low silver ion release and lack of adverse effects on cells in vitro. When GSAN were injected intravenously into mice without tumors, strong DEM contrast was observed in the heart and major blood vessels at 5 minutes post-injection (Figure 6A). These results indicated that detection of GSAN with DEM imaging was practical *in vivo*.

Next, we performed *in vivo* imaging with a mouse model of breast cancer. DEM images of representative tumor-bearing mice injected with either GSAN or iopamidol are presented in

Figure 6B. The DEM images of the mouse injected with GSAN show that there is an increased DEM signal in the tumor compared to the pre-injection scan. On the other hand, for mice injected with iopamidol, there was no substantial difference in the DEM signal observed in the tumors between pre- and post-injection scans at this time point (Figure 6C). The signal-to-noise ratios (SNR) in the tumors indicate that there was a substantial increase in DEM signal in the mice injected with GSAN at all post-injection time points (statistically significant at 30 and 120 min) compared to the SNR in the pre-injection scans (Figure 6C). However, for mice injected with iopamidol, no significant difference in the DEM signal was observed in the tumors at any time point. This is likely because iodine contrast agents have very low circulation half-lives and are quickly cleared from the body via renal excretion. While iodine contrast agents have been used for DEM in patients, the clearance is slower in humans than in mice. In our experiments, there was a delay of 1-2 minutes between the injection and first imaging time point, which may be sufficiently long enough for the agent to clear from the tumors in these mice. On the other hand, the GSAN are designed to have long circulation half-lives, and the enhanced permeability and retention (EPR) effect should therefore lead to accumulation in the tumor and increase the DEM signal over time.

In vivo imaging with CT

In addition to *in vivo* DEM imaging experiments, the *in vivo* CT contrast properties of GSAN were investigated using mice with and without breast tumors. CT images of a mouse without tumors that was injected with GSAN are shown in Figure 7A. Contrast was observed in the blood vessels over the imaging time points demonstrating that GSAN produce strong vascular contrast and have a long circulation half-life, as contrast was observed in the blood vessels over the imaging time points. Interestingly, contrast was also observed in the bladders and intestines of the mice (Figure 7A), which suggested that there is some excretion of the GSAN via urine and feces. In addition, CT imaging was done with a breast tumor mouse model and GSAN injections. The results suggested that GSAN can be used as a CT contrast agent for specific detection of breast cancers. In CT images of tumor-bearing mice, contrast was observed in the tumors significantly higher ($p < 0.05$) in all the post-injection scans compared to pre-injection scan (Figure 7B, C) and the intensity gradually increased over time (Figure 7B,C). This result is in agreement with the DEM imaging. Using this contrast agent (GSAN), CT could be used for breast cancer screening, which is relevant since several groups are developing CT scanners specifically for this purpose.[45,46] In addition, applications might exist for the detection of other tumor types such as lung cancer.[47]

We quantified the contrast in different organs over the various time points imaged. The contrast in the heart (i.e., the blood) was highest of all the organs (Figure 7C), and gradually declined over the two hour imaging time period. As is typical for nanoparticles, some accumulation in the liver and spleen was observed over time. The contrast observed in the bladder steadily increased over the imaging time period. The detection of contrast in the bladder was surprising, since the hydrodynamic size of the nanoparticles was 14 nm, larger than the expected renal filtration cut-off for nanoparticle excretion.[48] This observation motivated us to investigate excretion of the nanoparticles via ICP-OES, as described in the next section.

Biodistribution

The biodistribution of the Ag-60 GSAN formulation at 2 hours post-injection is presented in Figure 8 (this time point was selected to match the last in vivo imaging time point in order to confirm the excretion via the urine and feces observed via imaging). Higher amounts of gold and silver were found in the blood and spleen than in other tissues. More than 10% of the injected dose (ID) was still present in the blood, which suggested that these nanoparticles have a reasonably long circulation half-life. Around 5% of ID was found to be in the tumor, heart, lungs, and liver. Significant amounts of silver and gold were found in the urine and feces, which supports the CT imaging data, and indicates that GSAN are excreted from the body via urine and feces.

Conventional mammography has poor sensitivity for tumor detection in patients with dense breasts due to contrast produced by fibroglandular tissue.[4] In addition, women with dense breasts have a 3.25 higher risk of breast cancer, independent of issues related to screening.[49] Other techniques such as contrast-enhanced MRI have been proposed for breast cancer screening, but conventional MRI is not cost-effective to use routinely, is not applicable for many patients due to claustrophobia or contraindications such as metal implants, and has a high false positive rate.[50,51] Contrast-enhanced DEM is an emerging alternative to conventional mammography for screening of breast cancer. Contrast-enhanced DEM has the potential to reduce the contrast from healthy tissue and highlight tumors via use of contrast agents. The implementation of DEM is highly practical, since current FDA-approved DE mammography systems (Hologic and GE) involve only minor software and hardware upgrades to existing digital mammography equipment (installation of extra beam filters). As we discussed above, iodine-based agents are far from optimal for DEM. However, there has been only one contrast agent specifically developed for DEM reported to date.[18]

Silver is a more ideal material upon which to base DEM contrast agents than iodine,[8] and the development of silver-based contrast agents is an emerging field.[38,40,52] In this study we developed GSAN as a DEM contrast agent and more cost-effective blood pool CT contrast agent than AuNP. GSAN are composed of two noble metals (i.e., gold and silver). Silver contributes DEM and CT contrast, and inclusion of gold resulted in improved biocompatibility. GSAN have a long circulation time and significant amounts of GSAN accumulated in the tumor, producing DEM contrast. GSAN provided tumor contrast for longer periods of time compared to iodinated small molecules, as iodinated contrast agents have very short circulation half-lives. Our data show that GSAN are a promising contrast agent for DEM and may prove effective for the emerging technique of spectral mammography.[53]

CT phantom and *in vivo* CT images revealed that GSAN strongly attenuate x-rays. Gold nanoparticles have been proposed as blood pool CT contrast agents,[21,22] however gold is much more expensive than silver (the costs of silver and gold are $1.75/gram and $43.28/gram, respectively).[54,55] Making a CT contrast agent from a gold-silver alloy would reduce the cost of the agent, as silver is 30 times less expensive than gold. Interestingly, we observed that some of the GSAN (around 25% ID) was excreted from the body via the urine and feces, which is advantageous as FDA approval for a nanoparticle based contrast agent is likely dependent upon its excretion from the body. The fecal excretion is not unexpected and

such phenomena have been reported by others.[56,57] It is surprising that renal excretion was observed because the hydrodynamic diameter of the GSAN is 14 nm and prior reports have indicated that a hydrodynamic diameter below 5.5 nm is needed for renal excretion.[48] However, a fraction of this GSAN formulation may have hydrodynamic diameters less than 5 nm, therefore explaining this result.

Using GSAN as a contrast agent, CT could be used to detect tumors in other organs such as the lungs, where CT is frequently used for screening for cancer.[47] Future directions for this platform might include optimization of the synthesis to provide a formulation that can be entirely renally excreted via smaller core sizes and use of smaller surface-coating ligands such as glutathione.[58] Also GSAN could be encapsulated in polymeric nanoparticles or liposomes for improved circulation times[59,60] or together with therapeutic agents for image-guided therapy for different tumor types.

Conclusions

We have synthesized several gold-silver alloy nanoparticle formulations and demonstrated that inclusion of gold improved biocompatibility, but did not adversely affect the DEM contrast properties of the nanoparticles. The formation of gold-silver alloy nanoparticles reduced the leaching of silver ions from the GSAN compared to silver nanoparticles, thereby improving the biocompatibility. GSAN produced strong DEM and CT contrast in phantoms and *in vivo*. GSAN were found to produce strong vascular contrast in DEM and CT mouse imaging. Furthermore, we found that GSAN produced contrast in tumors using both these imaging techniques. The CT images of the mice and biodistribution results suggested that GSAN are excreted from the body via urine and feces. GSAN produced strong DEM and CT contrast in phantoms and *in vivo*, accumulate in tumors, and are biocompatible and excretable. Therefore GSAN have potential as DEM and CT contrast agents for breast cancer screening, and a blood pool CT contrast agent.

Materials and Methods

GSAN synthesis

GSAN were synthesized using a modified literature method.[61] A range of m-PEG capped GSAN formulations (termed Ag-100, Ag-90, Ag-80, Ag-70, Ag-60 and Ag-50) were synthesized by substituting several different percentages of silver nitrate with gold chloride (Table 1). In brief, 1.25 ml of 0.1 M sodium citrate dihydrate solution (Sigma-Aldrich, St. Louis, MO, USA) was added to a 1 liter conical flask containing 500 ml of DI water, which was stirring. Then different volumes of 0.1 M chloroauric acid trihydride (Sigma-Aldrich) and 0.1 M silver nitrate (Sigma-Aldrich) (described in Table 1) were added to the flask. 5 ml of 0.1 M sodium borohydride (Sigma-Aldrich) was then added to the reaction mixture. After 1 minute of vigorous stirring, 5 ml of 5 mg m-PEG/ml (molecular weight 2 kDa, Creative PEGWorks, Winston Salem, NC, USA) was added to the reaction mixture, which was then allowed to stir gently overnight. The resultant nanoparticles were concentrated and purified using 10 kDa molecular weight cut-off ultrafiltration tubes (Sartorius Stedim Biotech, Germany). The nanoparticles were washed thrice with PBS, concentrated and stored at 4 ºC for future use.

Characterization

Dynamic light scattering and zeta potential—The hydrodynamic diameters and zeta potentials of all the GSAN formulations were measured using a Zetasizer (Nano-ZS 90, Malvern instrument, Malvern, UK). In brief, 5 μl of GSAN from the stock were diluted with 4 ml of DI water. 1.5 ml and 1 ml of nanoparticle suspension were used for the measurement of hydrodynamic diameter and zeta potential, respectively. All the measurements were performed at 25 ºC.

UV/visible spectroscopy—UV/visible spectra of all GSAN formulations were recorded using a UV/visible spectrophotometer (Thermo-fisher scientific, USA). In brief, 5 μl from each GSAN stock were diluted with 2 ml of DI water. Since the stock concentrations ranged from 3.9 to 8.5 mg Ag/ml (Ag-50 to Ag-100), the diluted samples ranged from of 9.8 to 21.3 μg Ag/ml. The diluted samples were used to record UV-visible spectra. The absorbances of the GSAN were normalized such that the maximum absorbance for each sample was set to 1.

Inductively coupled plasma optical emission spectroscopy—The silver and gold concentrations in each GSAN formulation was determined using ICP-OES (Spectro Genesis ICP). In brief, 2.5, 5 and 10 μl of GSAN from stock of each formulation were placed into 15 ml falcon tubes. For the measurement of silver and gold concentration in each formulation, the nanoparticles were dissolved in 1 ml of concentrated nitric acid and 1 ml of aqua regia, respectively. Then the final volume in each tube was made to 10 ml with DI water. The concentrations obtained from the ICP-OES measurements were then multiplied by their dilution factor for each sample and averaged to obtain the final concentration of silver and gold in each formulation.

Transmission electron microscopy—TEM of all GSAN formulations was performed using a JEOL 1010 microscope operating at 80 kV. In brief, 10 μl of diluted GSAN formulations (10 μl from stock diluted with 500 μl DI water) was dropped onto carbon-coated copper grids (FCF-200-Cu, Electron Microscopy Sciences, Hatfield, PA, USA). The water was allowed to evaporate before imaging. The core diameter of each GSAN formulation was measured using ImageJ (National Institutes of Health, Bethesda, MD, USA).

Energy dispersive x-ray spectroscopy—A JEOL JEM-1400 transmission electron microscope (JEOL, MA. USA, Inc.) operating at an accelerating voltage of 120 kV was used to acquire energy dispersive X-ray spectroscopy (EDS) spectra from GSAN formulations. Briefly, one drop of aqueous dispersions of GSAN formulations was deposited on an ultrathin carbon type-A 400 mesh copper grid (Ted Pella Inc. CA. USA), and the droplet was then dried under ambient conditions. EDS spectra on each GSAN formulation were recorded.

Silver ion leaching

Silver ion leaching was investigated in two different media: DI water and simulated lysosomal fluid (citrate buffer at pH 5). The citrate buffer was composed of a mixture of

20.5 ml of 0.1 M citric acid and 29.5 ml of 0.1 M sodium citrate. We did not use media such as PBS or 10% serum in PBS for this study because these media contain chloride ions that form silver chloride precipitates with released silver ions, which is very challenging to separate from the silver nanoparticles. Any media that contains chloride ions is therefore confounding in silver ion release studies.[43] In brief, 50 μl (from 100 mg Ag/ml stock) from each formulation was added to 20 ml glass vials containing 4950 μl of DI water or simulated lysosomal fluid. The tubes were incubated at 37 °C. Samples from each formulation were collected at the following time intervals: 1, 2, 6, 24, 48, 72, 96, 120, 144 and 168 hours. The released silver ions were separated from GSAN by centrifuging the entire sample in 10 kDa molecular weight cut-off ultrafiltration tubes (Sartorius Stedim Biotech). 2.5 ml of filtrate was collected at each time point and fresh DI water or simulated lysosomal fluid was mixed with each sample. Then, the tubes were incubated at 37 °C until the next sample collection time point. The silver ion concentration in each filtrate was measured using ICP-OES. Three independent experiments were performed for each time point and formulation. The percentage cumulative silver ion released was calculated and the data presented as mean ± standard deviation (n=3).

Cell viability assay

Cell culture—J774A.1 (murine macrophage), Hep G2 (human hepatocellular liver carcinoma) and MDA-MB-231 (human breast cancer) cells were purchased from ATCC (Manassas, VA, USA). The Hep G2 cells were cultured in Eagle's Minimum Essential Medium, 10% fetal bovine serum (Gibco, Grand Island, NY USA), 45 IU/ml penicillin and 45 IU/ml streptomycin (Gibco). The J774A.1 and MDA-MB-231 cells were maintained in a culture medium of DMEM (ATCC), 10% FBS, 45 IU/ml penicillin and 45 IU/ml streptomycin (Gibco). The cells were grown at 37 °C in 5% CO_2 humidified incubator.

Cell viability assay—The cytotoxicity of each GSAN formulation was investigated in J774A.1 and Hep G2 cells using the MTS ((3-(4,5-dimethylthiazol-2-yl)-5-(3-carboxymethoxyphenyl)-2-(4-sulfophenyl)-2H-tetrazolium) assay (CellTiter 96 cell proliferation assay kit; Promega, Madison, WI, USA). The assay was performed in 96 well flat bottom microplates (Corning, NY, USA), according to previously published methods.[33] In brief, 10,000 cells were seeded in each well and the 96 well plate was incubated at 37 °C for 24 hours in a 5% CO_2 humidified incubator. After 24 hours of incubation, the cell monolayer was washed with sterile PBS and then incubated with GSAN dispersed in cell culture media at a dose of 200 μg Ag/ml for 2 and 24 hours. The silver exposure dose (200 μg Ag/ml) was kept constant for all formulations. Since the formulations contained a varying amount of gold, the number of nanoparticles was not constant in the assay, with Ag-50 containing 2.5 times the number of nanoparticles as Ag-100, for example. Six replicate wells were used for each control and test concentration per microplate. After 2 and 24 hours of incubation with GSAN, the cell monolayer was washed gently with sterile PBS twice. Then 20 μl of MTS/phenazine methosulfate (PMS) solution and 100 μl of cell culture medium were added to each well and the plates subsequently incubated at 37 °C for 1 hour. After this incubation, the absorbance was measured at 490 nm using a microplate reader. Three independent experiments were performed for each GSAN formulation. The percentage of

relative cell viability was calculated and the data presented as mean ± standard deviation (n=3).

Dual-energy mammography imaging

Dual-energy mammography imaging experiments were carried out using a Hologic Selenia Dimensions prototype system developed to perform DEM and DE tomosynthesis (Bedford, MA, USA). 0.30 mm copper and 0.05 mm silver filters were used for the HE and LE x-rays respectively. The LE images were acquired at 26 kV and 100 mAs, while the HE images were acquired at 45 kV and 40 mAs. The energies are chosen so that the k-edge of the contrast agent lies within the range spanned by the LE and HE x-ray spectra. The detector for the imaging system consists of a 0.5 mm selenium layer that is designed to improve the detection efficiency at higher energies. This system was used for both the phantom and mouse imaging experiments.

In the DE mouse imaging study, the HE image was registered to the LE image prior to image subtraction to correct for motion between image acquisitions. An intensity-based image registration algorithm from the Advanced Normalization Tools software package (Penn Image Computing & Science Lab, Philadelphia, PA, USA) was used. Large-scale motions were first corrected using a mutual information optimization and an affine transformation. Misalignments at finer scales were corrected using a normalized cross-correlation metric and diffeomorphic transform. This iterative hybrid registration approach is based on the multi-scale, deformable registration method for dual-energy x-ray images developed by Gang *et al.*[62] and was used as we have previously reported.[18,63] Image processing for the DE subtraction was then performed using MATLAB (MathWorks, Natick, MA, USA).

A weighted difference of the logarithms of the average LE and HE signal intensities (*SI)* is used to create a dual-energy (DE) image using

$$SI^{DE} = \ln\left(SI^{HE}\right) - w^{*}\ln\left(SI^{LE}\right) \quad (1)$$

where w is the weighting factor. This subtraction allows for the removal of background structures. More specifically, the weighting factor for the DE subtraction of the phantom w_{p} is given as a function of the average signal intensities of the adipose (a) and glandular (g) regions,

$$w_{\mathrm{p}} = \left[\ln\left(SI_a{}^{HE}\right) - \ln\left(SI_g{}^{HE}\right)\right] / \left[\ln\left(SI_a{}^{LE}\right) - \ln\left(SI_g{}^{LE}\right)\right] \quad (2)$$

The weighting factor for the DE subtraction of the mouse w_{m} is given as a function of the average signal intensities of the bone (b) and soft tissue (t) regions,

$$w_{\mathrm{m}} = \left[\ln\left(SI_b{}^{HE}\right) - \ln\left(SI_t{}^{HE}\right)\right] / \left[\ln\left(SI_b{}^{LE}\right) - \ln\left(SI_t{}^{LE}\right)\right] \quad (3)$$

Phantom imaging

Dual-energy mammography—A step phantom (Figure S5) was used to investigate the DEM contrast properties of the GSAN formulations.[8] The step phantom is composed of materials that attenuate x-rays similarly to breast tissues (from 100% glandular to 100 % adipose). This phantom is 3 cm high, 10 cm long and 4 cm wide. In brief, each GSAN formulation (the silver concentration was kept constant i.e. 16 mg Ag/ml for all GSAN) was loaded into a plastic tube and then the tube was inserted into a channel that had been bored through the step phantom. Tygon tubing was used (Fisher Scientific, ID = 3/32", OD = 5/32", wall = 1/32"). As a control, we also performed DEM phantom imaging with gold nanoparticles at both 16 and 50 mg/ml. These m-PEG capped gold nanoparticles were synthesized according to a previously reported protocol.[33] We used the 50 mg/ml concentration, which is 3 times more than the silver concentration used, as a robust test of whether AuNP produce significant DEM contrast. Then the step phantom containing GSAN or gold nanoparticles was scanned using high energy (HE) and low energy (LE) x-ray beams using the DE Hologic Selenia Dimensions prototype, as described above. A rectangular region of interest (ROI) was placed in each block of the DE subtraction images of the step phantom containing GSAN formulations or PBS. The DEM contrast from the 5 blocks was recorded and then averaged. The ROI size was the same for each block of the step phantom and for all GSAN formulations or PBS. Three images per GSAN formulation or PBS were analyzed. The CNR was determined using equation 4.

$$\mathrm{CNR} = [\mathrm{DEM\ contrast\ (GSAN)} - \mathrm{DEM\ contrast\ (PBS)}] \ / \ \mathrm{noise} \quad (4)$$

Statistical analysis on the CNR data was performed using unpaired Student's t-tests. Statistical significance among the groups was set at $p < 0.05$.

Computed tomography—A GSAN phantom was constructed according to a previously reported protocol.[23,24] In brief, different concentrations of GSAN (all formulations), iopamidol, silver and gold nanoparticles (from 0.5 mg/ml to 10 mg/ml total metal) were made. 300 μl of each agent was placed into PCR tubes and the tubes were secured in a plastic rack with parafilm. Three replicates for each agent and each concentration were included in the phantom. For the case of GSAN formulations, the mass of gold and silver combined was used as the concentration. The rack was immersed in a plastic container containing water 21 cm in height. The phantom was scanned using a Siemens SOMATOM Force 192-slice clinical CT scanner at 80, 100, 120 and 140 kV, with a matrix size of 512 × 512, slice thickness of 0.5 cm and field of view 37 × 37 cm. The convolution kernel Br 40d and an x-ray tube current of 360 mA was used for each voltage. The images were analyzed using Osirix 64 bit (v3.7.1). The attenuation value in Hounsfield units (HU) for each sample tube was determined from three different slices and averaged for each sample. The data are presented as CT attenuation rate (HU/mg) of different agents (mean ± SD; n=3).

In vivo imaging

Animal experiments—In vivo experimental protocols were approved by the Institutional Animal Care and Use Committee (IACUC) of the University of Pennsylvania. Imaging experiments were performed using mice with and without breast tumors (n=4/group). To create the breast cancer model, nude female mice were inoculated with MDA-MB-231 cells in their mammary glands. Four million MDA-MB-231 cells were inoculated into each mammary gland. Imaging was performed at 3 weeks post-injection, and the tumor volumes of the mice were approximately 100 mm^3 at this time. All *in vivo* experiments were performed with GSAN (Ag-60) at a dose of 250 mg Ag/kg administered via the tail vein. As a control, we used a clinically-approved iodinated contrast agent, iopamidol (ISOVUE-300, Braco Diagnostic), at a dose of 250 mg I/kg. The iopamidol dose used is comparable to that used clinically.[64,65] Of note, iopamidol contains three iodine atoms per molecule. All animal imaging experiments were performed under isoflurane anesthesia.

In vivo DEM imaging—We used the aforementioned Hologic Selenia Dimensions DEM prototype for *in vivo* imaging experiments. We first imaged mice without tumors in order to test whether we could observe contrast from the GSAN agents *in vivo*. Next, we imaged tumor-bearing mice (the model is described above) to investigate the ability of the nanoparticles to create contrast in tumors. The mice were scanned at several time points: pre-injection, immediately post-injection, 30, 60 and 120 minutes. Mice were scanned with two different energies i.e. high energy (45 kV) and low energy (26 kV). The DEM signal in the tumors was calculated using ImageJ. An oval ROI was placed on the tumor area in each DE subtraction image of mice injected with GSAN or iopamidol at each time point. The ROI size was the same for all mice injected with GSAN or iopamidol. Three images per mouse and four mice per group were analyzed. The SNR in the tumors of each mouse was calculated using equation (4). The data are presented as mean ±SD. Statistical analysis of the SNR data was performed using unpaired t-tests. Statistical significance among the groups set at $p < 0.05$.

$$\mathrm{SNR} = \mu^{\mathrm{sig}} / \sigma^{\mathrm{bg}} \quad (5)$$

where μ_{sig} is the average signal value in the tumor, and σ_{bg} is the standard deviation of the background.

In vivo CT imaging—CT imaging experiments were performed using a MicroCAT II (Imtek, Inc, Knoxville, TN, USA). Mice without tumors (n=4) were used to investigate the vascular contrast from the GSAN, whereas mice with tumors were used to investigate the feasibility of using GSAN as a CT contrast agent for breast cancer diagnosis. Mice were scanned prior to injection and at 5, 30, 60 and 120 minutes post-injection. CT images were acquired using the following parameters: slice thickness 100 μm, field of view 51.2 mm × 76.8 mm, tube voltage 80 kV and tube current 500 μA. The reconstruction kernel used a Feldkamp cone beam correction and a Shepp-Logan filter. The CT images were analyzed using Osirix 64 bit (v3.7.1). The attenuation values in Hounsfield units (HU) for several

organs (i.e., heart, liver, spleen, bladder and tumor) were recorded from three different slices and averaged. The data is presented as the change in attenuation compared to pre-injection scan (mean ± SEM).

Biodistribution of GSAN

The biodistribution of GSAN (Ag-60) was investigated in mice with and without tumors (n=4/group). Mice were divided into two groups, group-1 for silver and group-2 for gold measurement. Different mice were used due to technical issues for measuring gold and silver content from a single tissue sample. For gold measurements, tissue must be digested with a combination of nitric acid and hydrochloric acid. As silver and hydrochloric acid reacts to form silver chloride precipitate, silver content could not be measured in these samples, and so we used additional groups of mice to determine the biodistribution of silver. 2 hours after injection with GSAN, the mice were sacrificed, blood and urine samples were collected, and the mice were then perfused via the left ventricle with 20 ml PBS. After perfusion, the liver, lungs, heart, spleen, kidneys and fecal materials from the large intestine were collected. Tumors were collected from separate groups of tumor-bearing mice at 2 hours post-injection with GSAN that had not been perfused. All the organs and tumors were weighed and then minced into small pieces. The tissues were digested in 1 ml of concentrated nitric acid at 75 ºC for 16 hours to measure the silver content. To measure the gold content in the tissues, the tissues were digested in 800 µl of concentrated nitric acid at 75 ºC for 16 hours and then 200 µl of concentrated hydrochloric acid was added. The silver and gold content in each sample was determined using the ICP-OES. Data are presented as mean ± SD.

Statistical analysis

All the experiments were performed at least in triplicate (three independent experiments). Statistical analysis was carried out via unpaired t-tests using GraphPad Prism 5 software.

Supplementary Material

Refer to Web version on PubMed Central for supplementary material.

Acknowledgements

This work was supported by funding from NIH grants R00 EB012165, R03-CA171661, R01 HL131557 and startup funds from the University of Pennsylvania (all DPC). This work was supported by the National Center for Research Resources and the National Center for Advancing Translational Sciences, National Institutes of Health, through grant UL1TR000003. The project described was supported in part by Grant Number UL1RR024134 from the National Center for Research Resources. The content is solely the responsibility of the authors and does not necessarily represent the official views of the NIH. This work is also supported in part by the Institute for Translational Medicine and Therapeutics' (ITMAT) Transdisciplinary Program in Translational Medicine and Therapeutics. The prototype imaging system is provided to Penn by Hologic (Bedford, MA) under a research agreement. This work was also supported by a Komen leadership grant, AC140060, a Department of Energy training grant, DE-SE0012476 and an American Roentgen Ray Society Scholar (all ESM).

References

1. Elmore JG, Armstrong K, Lehman CD, Fletcher SW. Screening for breast cancer. JAMA. 2005; 293(10):1245–56. [PubMed: 15755947]
2. Screening for breast cancer: U.S. Preventive Services Task Force recommendation statement. Ann Intern Med. 2009; 151(10):716–26. W-236. [PubMed: 19920272]

3. Jochelson MS, Dershaw DD, Sung JS, Heerdt AS, Thornton C, Moskowitz CS, Ferrara J, Morris EA. Bilateral contrast-enhanced dual-energy digital mammography: feasibility and comparison with conventional digital mammography and MR imaging in women with known breast carcinoma. Radiology. 2013; 266(3):743–51. [PubMed: 23220903]
4. Dromain C, Thibault F, Diekmann F, Fallenberg EM, Jong RA, Koomen M, Hendrick RE, Tardivon A, Toledano A. Dual-energy contrast-enhanced digital mammography: initial clinical results of a multireader, multicase study. Breast Cancer Res. 2012; 14(3)
5. Sickles EA. The use of breast imaging to screen women at high risk for cancer. Radiol Clin North Am. 2010; 48(5):859–78. [PubMed: 20868890]
6. Jochelson M. Radiol Clin North Am. 2014; 52(3):609–16. [PubMed: 24792660]
7. Wang AT, Vachon CM, Brandt KR, Ghosh K. Contrast-enhanced digital mammography. Mayo Clin Proc. 2014; 89(4):548–57. [PubMed: 24684876]
8. Karunamuni R, Tsourkas A, Maidment AD. Exploring silver as a contrast agent for contrast-enhanced dual-energy X-ray breast imaging. Br J Radiol. 2014; 87(1041):20140081. [PubMed: 24998157]
9. Yu SB, Watson AD. Metal-Based X-ray Contrast Media. Chem Rev. 1999; 99(9):2353–78. [PubMed: 11749484]
10. Jun YW, Huh YM, Choi JS, Lee JH, Song HT, Kim S, Yoon S, Kim KS, Shin JS, Suh JS, Cheon J. Nanoscale size effect of magnetic nanocrystals and their utilization for cancer diagnosis via magnetic resonance imaging. J Am Chem Soc. 2005; 127(16):5732–3. [PubMed: 15839639]
11. Stacul F, van der Molen AJ, Reimer P, Webb JAW, Thomsen HS, Morcos SK, Almen T, Aspelin P, Bellin MF, Clement O, Heinz-Peer G. Contrast induced nephropathy: updated ESUR Contrast Media Safety Committee guidelines. Euro Radiol. 2011; 21(12):2527–2541.
12. Solomon R, Dumouchel W. Contrast media and nephropathy: findings from systematic analysis and Food and Drug Administration reports of adverse effects. Invest Radiol. 2006; 41(8):651–60. [PubMed: 16829749]
13. Tepel M, Aspelin P, Lameire N. Contrast-induced nephropathy: a clinical and evidence-based approach. Circulation. 2006; 113(14):1799–806. [PubMed: 16606801]
14. Artemov D, Mori N, Okollie B, Bhujwalla ZM. MR molecular imaging of the Her-2/neu receptor in breast cancer cells using targeted iron oxide nanoparticles. Magn. Reson. Med. 2003; 49:403–8. [PubMed: 12594741]
15. Balasundaram G, Ho CJ, Li K, Driessen W, Dinish US, Wong CL, Ntziachristos V, Liu B, Olivo M. Molecular photoacoustic imaging of breast cancer using an actively targeted conjugated polymer. Int J Nanomedicine. 2015; 10:387–97. [PubMed: 25609951]
16. Chow EK-H, Ho D. Cancer Nanomedicine: From Drug Delivery to Imaging. Sci. Transl. Med. 2013; 5:216rv4–216rv4.
17. Kinsella JM, Jimenez RE, Karmali PP, Rush AM, Kotamraju VR, Gianneschi NC, Ruoslahti E, Stupack D, Sailor MJ. X-ray computed tomography imaging of breast cancer by using targeted peptide-labeled bismuth sulfide nanoparticles. Angew. Chem. Int. Ed. 2011; 50:12308–11.
18. Karunamuni R, Naha PC, Lau KC, Al-Zaki A, Popov AV, Delikatny EJ, Tsourkas A, Cormode DP, Maidment AD. Development of silica-encapsulated silver nanoparticles as contrast agents intended for dual-energy mammography. Eur Radiol. 2016 (on line).
19. Cormode DP, Naha PC, Fayad ZA. Nanoparticle contrast agents for computed tomography: a focus on micelles. Contrast Media Mol Imaging. 2014; 9(1):37–52. [PubMed: 24470293]
20. Arifin DR, Long CM, Gilad AA, Alric CE, Roux S, Tillement O, Link TW, Arepally A, Bulte JWM. Trimodal Gadolinium-Gold Microcapsules Containing Pancreatic Islet Cells Restore Normoglycemia in Diabetic Mice and Can Be Tracked by Using US, CT, and Positive-Contrast MR Imaging. Radiology. 2011; 260(3):790–798. [PubMed: 21734156]
21. Cai QY, Kim SH, Choi KS, Kim SY, Byun SJ, Kim KW, Park SH, Juhng SK, Yoon KH. Colloidal gold nanoparticles as a blood-pool contrast agent for X-ray computed tomography in mice. Invest Radiol. 2007; 42(12):797–806. [PubMed: 18007151]
22. Cormode DP, Skajaa T, van Schooneveld MM, Koole R, Jarzyna P, Lobatto ME, Calcagno C, Barazza A, Gordon RE, Zanzonico P, Fisher EA, Fayad ZA, Mulder WJ. Nanocrystal core high-

density lipoproteins: a multimodality contrast agent platform. Nano Lett. 2008; 8(11):3715–23. [PubMed: 18939808]

23. Brown AL, Naha PC, Benavides-Montes V, Litt HI, Goforth AM, Cormode DP. Synthesis, X-ray Opacity, and Biological Compatibility of Ultra-High Payload Elemental Bismuth Nanoparticle X-ray Contrast Agents. Chem Mater. 2014; 26(7):2266–2274. [PubMed: 24803727]
24. Naha PC, Zaki AA, Hecht E, Chorny M, Chhour P, Blankemeyer E, Yates DM, Witschey WR, Litt HI, Tsourkas A, Cormode DP. Dextran coated bismuth-iron oxide nanohybrid contrast agents for computed tomography and magnetic resonance imaging. J Mater Chem B. 2014; 2(46):8239–8248.
25. Cole LE, Ross RD, Tilley JM, Vargo-Gogola T, Roeder RK. Gold nanoparticles as contrast agents in x-ray imaging and computed tomography. Nanomedicine (Lond). 2015; 10(2):321–41. [PubMed: 25600973]
26. Rabin O, Manuel Perez J, Grimm J, Wojtkiewicz G, Weissleder R. An X-ray computed tomography imaging agent based on long-circulating bismuth sulphide nanoparticles. Nat Mater. 2006; 5(2):118–22. [PubMed: 16444262]
27. Allijn IE, Leong W, Tang J, Gianella A, Mieszawska AJ, Fay F, Ma G, Russell S, Callo CB, Gordon RE, Korkmaz E, Post JA, Zhao YM, Gerritsen HC, Thran A, Proksa R, Daerr H, Storm G, Fuster V, Fisher EA, Fayad ZA, Mulder WJM, Cormode DP. Nanocrystal Labeling Allows Low-Density Lipoprotein Imaging from the Subcellular to Macroscopic Level. Acs Nano. 2013; 7(11): 9761–9770. [PubMed: 24127782]
28. Galper MW, Saung MT, Fuster V, Roessl E, Thran A, Proksa R, Fayad ZA, Cormode DP. Effect of Computed Tomography Scanning Parameters on Gold Nanoparticle and Iodine Contrast. Invest Radiol. 2012; 47(8):475–481. [PubMed: 22766909]
29. Hill ML, Gorelikov I, Niroui F, Levitin RB, Mainprize JG, Yaffe MJ, Rowlands JA, Matsuura. Towards a nanoscale mammographic contrast agent: development of a modular pre-clinical dual optical/x-ray agent. N. Phys Med Biol. 2013; 58(15):5215–35.
30. Blasi F, Oliveira BL, Rietz TA, Rotile NJ, Day H, Naha PC, Cormode DP, Izquierdo-Garcia D, Catana C, Caravan P. Radiation Dosimetry of the Fibrin-Binding Probe Cu-64-FBP8 and Its Feasibility for PET Imaging of Deep Vein Thrombosis and Pulmonary Embolism in Rats. J. Nucl. Med. 2015; 56(7):1088–1093. [PubMed: 25977464]
31. Blasi F, Oliveira BL, Rietz TA, Rotile NJ, Naha PC, Cormode DP, Izquierdo-Garcia D, Catana C, Caravan P. Multisite Thrombus Imaging and Fibrin Content Estimation With a Single Whole-Body PET Scan in Rats. Arterioscler. Thromb. Vasc.Biol. 2015; 35(10):2114–2121. [PubMed: 26272938]
32. Thakor AS, Jokerst J, Zavaleta C, Massoud TF, Gambhir SS. Gold nanoparticles: a revival in precious metal administration to patients. Nano Lett. 2011; 11(10):4029–36. [PubMed: 21846107]
33. Naha PC, Chhour P, Cormode DP. Systematic in vitro toxicological screening of gold nanoparticles designed for nanomedicine applications. Toxicol. In Vitro. 2015; 29(7):1445–1453. [PubMed: 26031843]
34. Libutti SK, Paciotti GF, Byrnes AA, Alexander HR, Gannon WE, Walker M, Seidel GD, Yuldasheva N, Tamarkin L. Phase I and Pharmacokinetic Studies of CYT-6091, a Novel PEGylated Colloidal Gold-rhTNF Nanomedicine. Clin. Cancer Res. 2010; 16(24):6139–6149. [PubMed: 20876255]
35. van der Zande M, Vandebriel RJ, Van Doren E, Kramer E, Herrera Rivera Z, Serrano-Rojero CS, Gremmer ER, Mast J, Peters RJ, Hollman PC, Hendriksen PJ, Marvin HJ, Peijnenburg AA, Bouwmeester H. Distribution, elimination, and toxicity of silver nanoparticles and silver ions in rats after 28-day oral exposure. ACS Nano. 2012; 6(8):7427–42. [PubMed: 22857815]
36. Khlebtsov N, Dykman L. Biodistribution and toxicity of engineered gold nanoparticles: a review of in vitro and in vivo studies. Chem. Soc. Rev. 2011; 40:1647–71. [PubMed: 21082078]
37. Gheorghe DE, Cui L, Karmonik C, Brazdeikis A, Penaloza JM, Young JK, Drezek RA, Bikram M. Gold-silver alloy nanoshells: a new candidate for nanotherapeutics and diagnostics. Nanoscale Res. Lett. 2011; 6:554. [PubMed: 21995302]

38. Huo D, Ding J, Cui YX, Xia LY, Li H, He J, Zhou ZY, Wang HW, Hu Y. X-ray CT and pneumonia inhibition properties of gold-silver nanoparticles for targeting MRSA induced pneumonia. Biomaterials. 2014; 35:7032–41. [PubMed: 24836950]
39. Huo D, He J, Li H, Yu H, Shi T, Feng Y, Zhou Z, Hu Y. Fabrication of Au@Ag core-shell NPs as enhanced CT contrast agents with broad antibacterial properties. Colloids Surf. B. 2014; 117:29–35.
40. Zou J, Hannula M, Misra S, Feng H, Labrador RH, Aula AS, Hyttinen J, Pyykko I. Micro CT visualization of silver nanoparticles in the middle and inner ear of rat and transportation pathway after transtympanic injection. J. Nanobiotechnology. 2015; 13:5. [PubMed: 25622551]
41. Ferrando R, Jellinek J, Johnston RL. Nanoalloys: from theory to applications of alloy clusters and nanoparticles. Chem Rev. 2008; 108(3):845–910. [PubMed: 18335972]
42. Kittler S, Greulich C, Diendorf J, Koller M, Epple M. Toxicity of Silver Nanoparticles Increases during Storage Because of Slow Dissolution under Release of Silver Ions. Chem Mater. 2010; 22(16):4548–4554.
43. Loza K, Diendorf J, Sengstock C, Ruiz-Gonzalez L, Gonzalez-Calbet JM, Vallet-Regi M, Koller M, Epple M. The dissolution and biological effects of silver nanoparticles in biological media. J Mater Chem B. 2014; 2(12):1634–1643.
44. Karunamuni R, Maidment AD. Search for novel contrast materials in dual-energy x-ray breast imaging using theoretical modeling of contrast-to-noise ratio. Phys. Med. Biol. 2014; 59:4311–24. [PubMed: 25029534]
45. Lindfors KK, Boone JM, Nelson TR, Yang K, Kwan AL, Miller DF. Dedicated breast CT: initial clinical experience. Radiology. 2008; 246(3):725–33. [PubMed: 18195383]
46. Prionas ND, Lindfors KK, Ray S, Huang SY, Beckett LA, Monsky WL, Boone JM. Contrast-enhanced dedicated breast CT: initial clinical experience. Radiology. 2010; 256(3):714–23. [PubMed: 20720067]
47. Aberle DR, Adams AM, Berg CD, Black WC, Clapp JD, Fagerstrom RM, Gareen IF, Gatsonis C, Marcus PM, Sicks JD. Reduced lung-cancer mortality with low-dose computed tomographic screening. N. Engl. J. Med. 2011; 365(5):395–409. [PubMed: 21714641]
48. Choi HS, Liu W, Misra P, Tanaka E, Zimmer JP, Itty Ipe B, Bawendi MG, Frangioni JV. Renal clearance of quantum dots. Nat Biotechnol. 2007; 25(10):1165–70. [PubMed: 17891134]
49. McCormack VA, dos Santos Silva I. Breast density and parenchymal patterns as markers of breast cancer risk: a meta-analysis. Cancer Epidemiol. Biomarkers Prev. 2006; 15(6):1159–69. [PubMed: 16775176]
50. Berg WA, Zhang Z, Lehrer D, Jong RA, Pisano ED, Barr RG, Bohm-Velez M, Mahoney MC, Evans WP, Larsen LH, Morton MJ, Mendelson EB, Farria DM, Cormack JB, Marques HS, Adams A, Yeh NM, Gabrielli G, Investigators, A. Detection of Breast Cancer With Addition of Annual Screening Ultrasound or a Single Screening MRI to Mammography in Women With Elevated Breast Cancer Risk. JAMA. 2012; 307(13):1394–1404. [PubMed: 22474203]
51. Ho JM, Jafferjee N, Covarrubias GM, Ghesani M, Handler B. Dense breasts: a review of reporting legislation and available supplemental screening options. AJR Am J Roentgenol. 2014; 203(2): 449–56. [PubMed: 25055284]
52. Shi J, Wang L, Zhang J, Ma R, Gao J, Liu Y, Zhang C, Zhang Z. A tumor-targeting near-infrared laser-triggered drug delivery system based on GO@Ag nanoparticles for chemo-photothermal therapy and X-ray imaging. Biomaterials. 2014; 35:5847–61. [PubMed: 24746963]
53. Fallenberg EM, Dromain C, Diekmann F, Engelken F, Krohn M, Singh JM, Ingold-Heppner B, Winzer KJ, Bick U, Renz DM. Contrast-enhanced spectral mammography versus MRI: Initial results in the detection of breast cancer and assessment of tumour size. Eur Radiol. 2014; 24(1): 256–64. [PubMed: 24048724]
54. Gold price. http://goldprice.org.(accessed on May 2016)
55. Silver price. http://silverprice.org. (accessed on May 2016)
56. Bulte JW, Schmieder AH, Keupp J, Caruthers SD, Wickline SA, Lanza GM. MR cholangiography demonstrates unsuspected rapid biliary clearance of nanoparticles in rodents: implications for clinical translation. Nanomedicine. 2014; 10(7):1385–8. [PubMed: 24832959]

57. Skajaa T, Cormode DP, Jarzyna PA, Delshad A, Blachford C, Barazza A, Fisher EA, Gordon RE, Fayad ZA, Mulder WJ. The biological properties of iron oxide core high-density lipoprotein in experimental atherosclerosis. Biomaterials. 2011; 32(1):206–13. [PubMed: 20926130]
58. Simpson CA, Salleng KJ, Cliffel DE, Feldheim DL. In vivo toxicity, biodistribution, and clearance of glutathione-coated gold nanoparticles. Nanomedicine. 2013; 9(2):257–63. [PubMed: 22772047]
59. Chhour P, Gallo N, Cheheltani R, Williams D, Al-Zaki A, Paik T, Nichol JL, Tian Z, Naha PC, Witschey WR, Allcock HR, Murray CB, Tsourkas A, Cormode DP. Nanodisco balls: control over surface versus core loading of diagnostically active nanocrystals into polymer nanoparticles. ACS Nano. 2014; 8(9):9143–53. [PubMed: 25188401]
60. Mukundan S Jr. Ghaghada KB, Badea CT, Kao CY, Hedlund LW, Provenzale JM, Johnson GA, Chen E, Bellamkonda RV, Annapragada A. A liposomal nanoscale contrast agent for preclinical CT in mice. AJR Am J Roentgenol. 2006; 186(2):300–7. [PubMed: 16423931]
61. Mallin MP, Murphy CJ. Solution-phase synthesis of sub-10 nm Au-Ag alloy nanoparticles. Nano Lett. 2002; 2(11):1235–1237.
62. Gang GJ, Varon CA, Kashani H, Richard S, Paul NS, Van Metter R, Yorkston J, Siewerdsen JH. Multiscale deformable registration for dual-energy x-ray imaging. Med Phys. 2009; 36(2):351–63. [PubMed: 19291974]
63. Lau KC, Roth S, Maidment ADA. 2D and 3D registration methods for dual-energy contrast-enhanced digital breast tomosynthesis. Proc. SPIE Medical Imaging. 2014 doi: 10.1117/12.2044080.
64. Halpern EJ, Gingold EL, White H, Read K. Evaluation of coronary artery image quality with knowledge-based iterative model reconstruction. Academic Radiol. 2014; 21:805–11.
65. Luczynska E, Heinze-Paluchowska S, Hendrick E, Dyczek S, Rys J, Herman K, Blecharz P, Jakubowicz J. Comparison between Breast MRI and Contrast-Enhanced Spectral Mammography. Med. Sci. Monit. 2015; 21:1358–1367. [PubMed: 25963880]

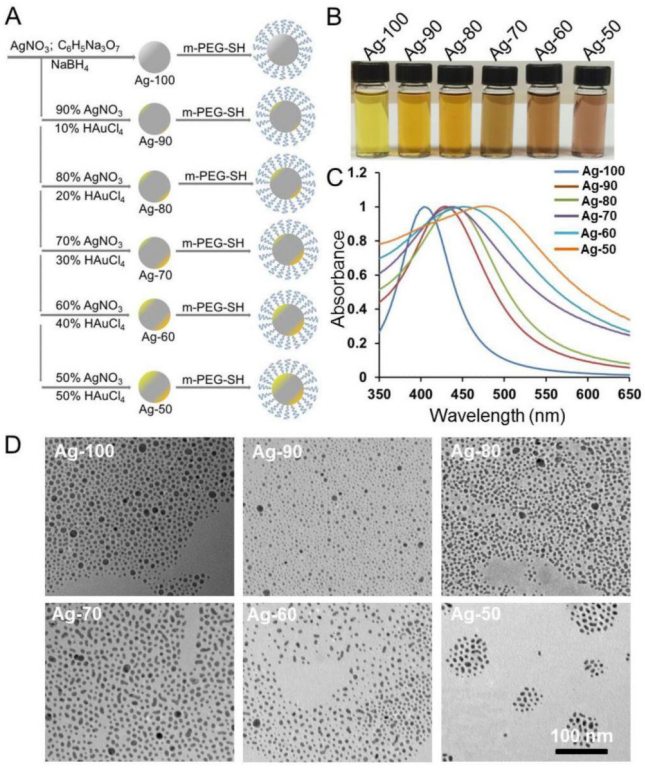

Figure 1.

A) Schematic depiction of GSAN synthesis. B) A photo of GSAN formulations. C) UV-visible spectra of GSAN formulations. D) TEM images of GSAN formulations (scale is the same in all panels).

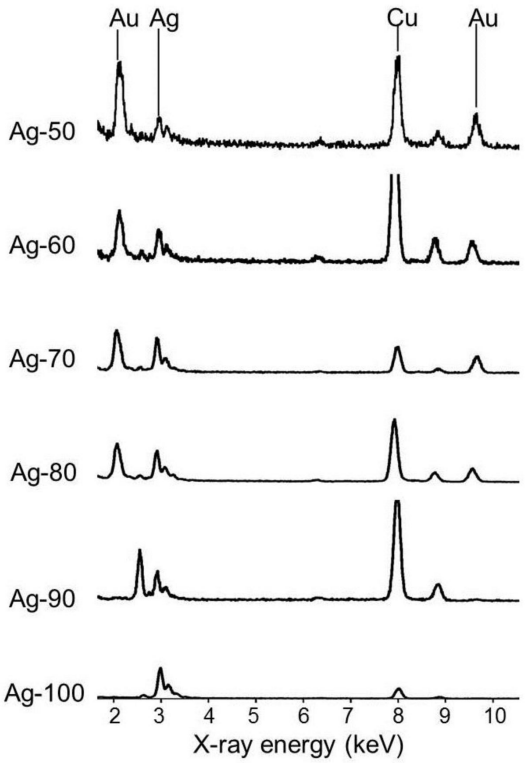

Figure 2.
Energy dispersive x-ray spectra of GSAN formulations. The graphs are normalized to the height of the silver peak.

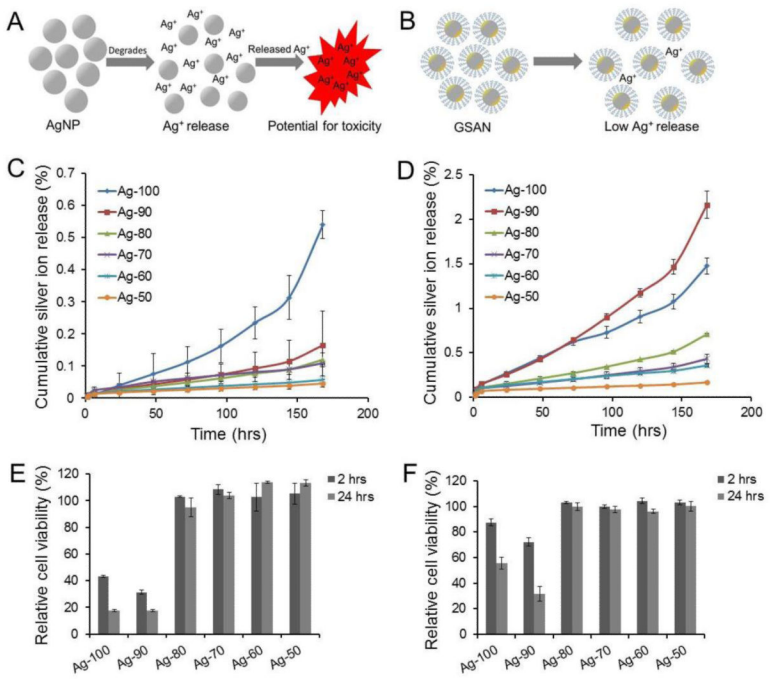

Figure 3.

Schematics showing (A) leaching of silver ions from the silver nanoparticles and (B) GSAN not leaching silver ions. Silver ion release from different formulations (C) in DI water and (D) in simulated lysosomal fluid. Cell viability of (E) J774A.1 and (F) Hep G2 cells, when incubated with GSAN.

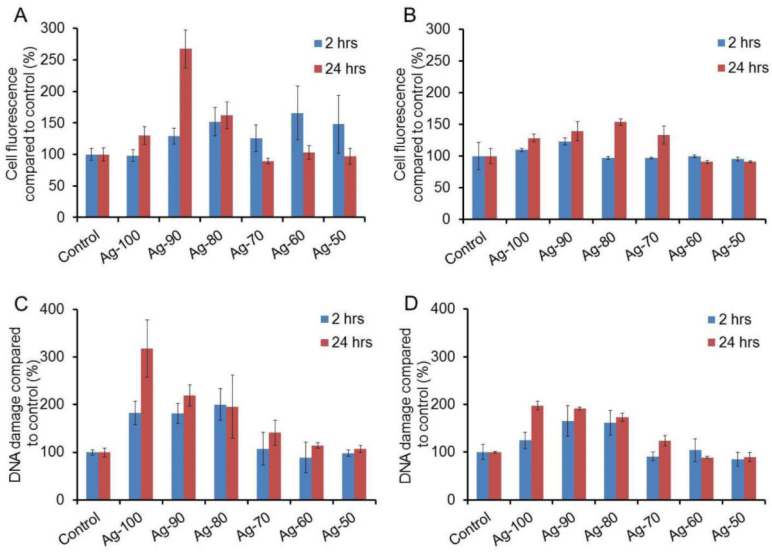

Figure 4.

Reactive oxygen species generation in (A) J774A.1 and (B) Hep G2 cells, when incubated with GSAN. Evaluation of DNA damage effects of GSAN with J774A.1 (C) and Hep G2 (D) cells.

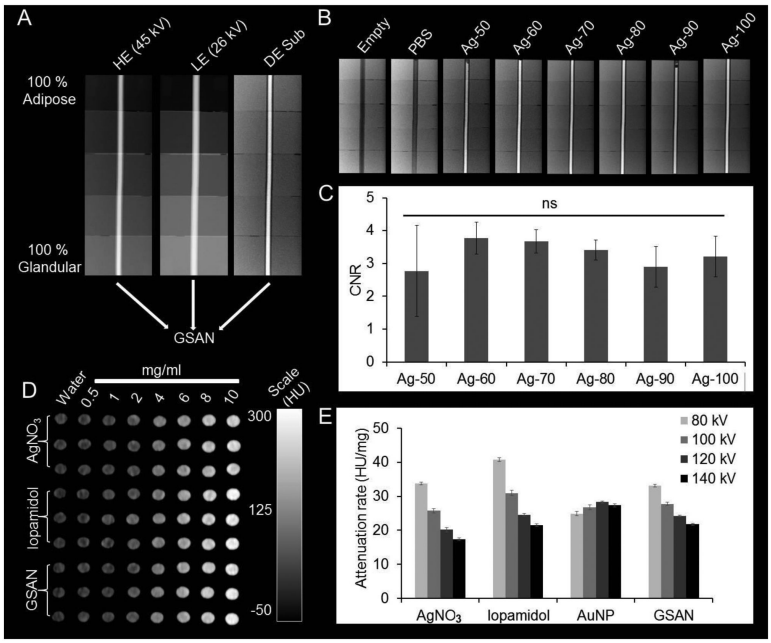

Figure 5.

Phantom imaging with DEM and CT. A) HE, LE and DE images of a step phantom containing GSAN scanned with a DEM system. B) DE subtraction images of step phantom containing GSAN formulations and controls. The silver concentration was kept constant i.e. 16 mg Ag/ml for all GSAN formulation. C) Quantification of DEM phantom data. (n.s. = non-significant). D) CT phantom images of silver nitrate, iopamidol, and GSAN (Ag-80) scanned at 120 kV (in the case of GSAN, the concentration is given as the mass of silver and gold); E) CT attenuation rates of different agents.

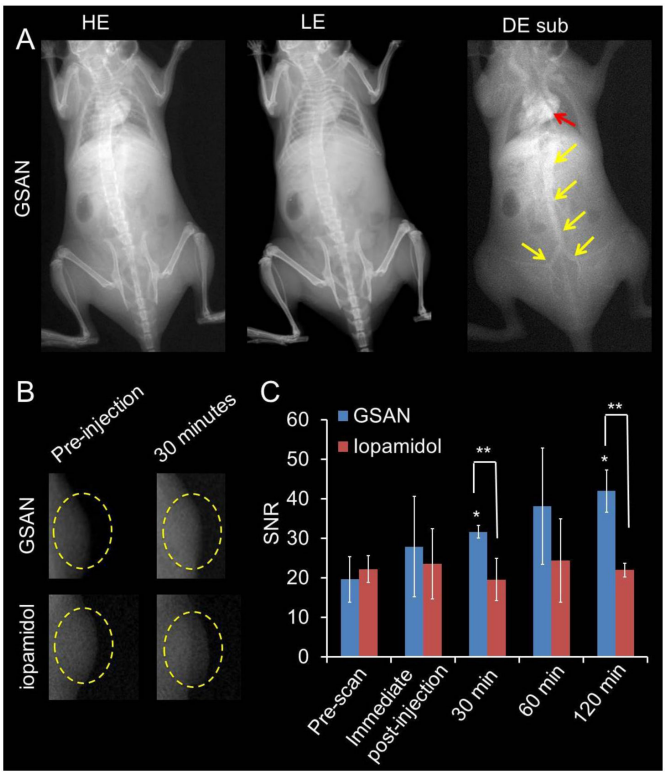

Figure 6.

In vivo DEM imaging with GSAN and iodine. A) DEM images of a mouse (without a tumor) injected with GSAN. DEM images aquired at 5 minutes post-injection. Red and yellow arrows indicates DEM contrast in the heart and blood vessels respectively. B) DEM images of representative tumor-bearing mice pre-injection and at 30 minutes post-injection with GSAN or iopamidol. The yellow circles indicate tumors. C) SNR in the tumors at different time points. Error bars are standard deviations. * indicates statistically significant between pre- and post-injection scan ($p < 0.05$); ** indicates statistically significant between GSAN and iopamidol ($p < 0.05$).

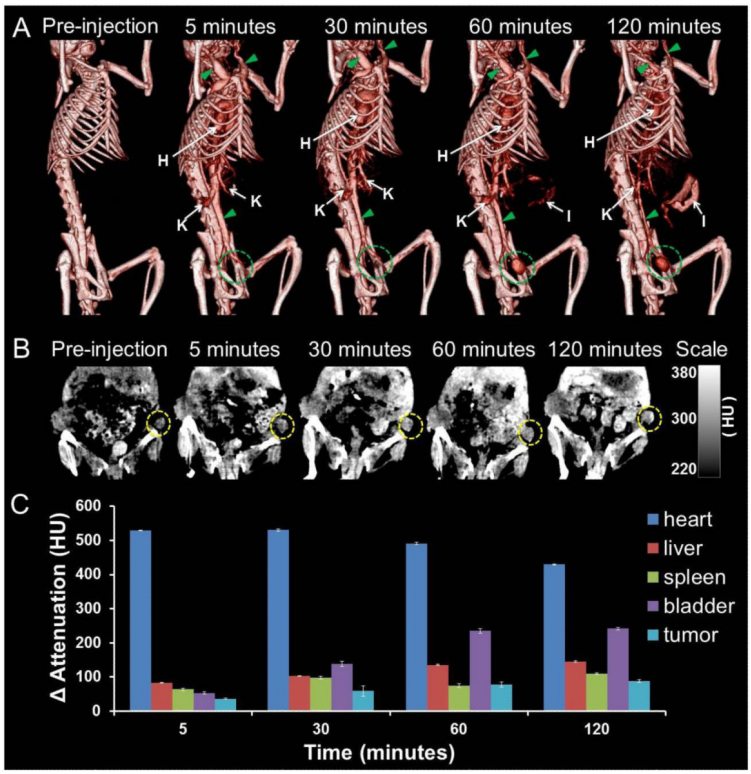

Figure 7.

In vivo CT imaging with GSAN. A) 3D volume rendered CT images of a mouse (without a tumor) injected with GSAN. Green arrowheads indicate blood vessels and green circles indicate the bladder. Hearts, kidneys, intestines and bladders are labeled H, K, I and B, respectively. B) 2D CT images of a tumor-bearing mouse showing accumulation of GSAN in the tumors at different time points. Yellow circles indicate tumors. C) Quantification of CT attenuation in different organs of mice injected with GSAN at different time points. Error bars are standard error of mean.

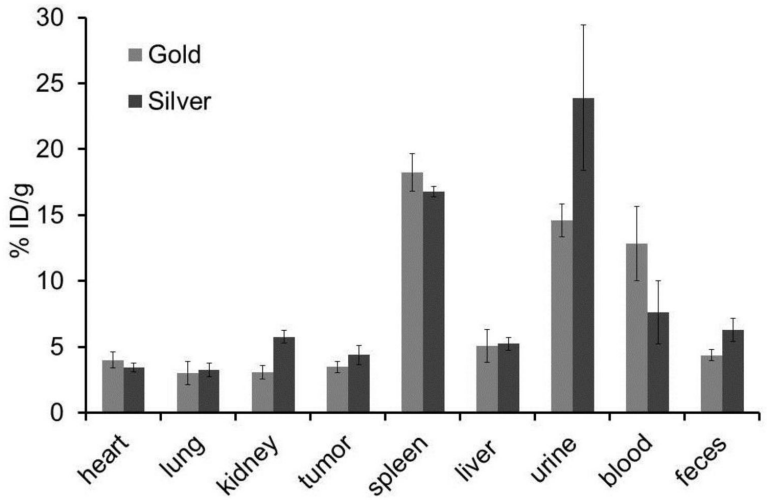

Figure 8.
Biodistribution of GSAN (Ag-60) in different organs at 2 hours post-injection.

Table 1

Synthesis and characterization data for GSAN formulations.

Formulation	0.1 M AgNO3 (μl)	0.1 M $HAuCl_4 . 3H_2O$ (μl)	Hydrodynamic diameter (nm)	Core diameter (nm)	Zeta potential (mV)	Molar ratio (Ag/Au)	Molar (%) Ag	% yield (Ag)
Ag-100	1250	0	13 ± 2	7.6 ± 2.8	−18.1 ± 1.9	-	-	63
Ag-90	1125	125	16 ± 1	3.6 ± 1.4	−19.3 ± 2.8	5.97	85.6	68
Ag-80	1000	250	16 ± 5	4.7 ± 2.3	−21.5 ± 2.7	2.41	70.6	69
Ag-70	875	375	17 ± 2	6.4 ± 1.7	−19.6 ± 1.3	1.74	63.5	70
Ag-60	750	500	14 ± 3	4.6 ± 1.4	−20.0 ± 1.8	1.08	51.9	70
Ag-50	625	625	16 ± 4	5.7 ± 1.5	−20.2 + 1.1	0.66	39.7	58